

Generative Regression for Left Ventricular Ejection Fraction Estimation from Echocardiography Video

Jinrong Lv, Xun Gong *Member, IEEE*, Zhaoquan Li, and Weili Jiang

Abstract—Estimating Left Ventricular Ejection Fraction (LVEF) from echocardiograms constitutes an ill-posed inverse problem. Inherent noise, artifacts, and limited viewing angles introduce ambiguity, where a single video sequence may map not to a unique ground truth, but rather to a distribution of plausible physiological values. Prevailing deep learning approaches typically formulate this task as a standard regression problem that minimizes the Mean Squared Error (MSE). However, this paradigm compels the model to learn the conditional expectation, which may yield misleading predictions when the underlying posterior distribution is multimodal or heavy-tailed—a common phenomenon in pathological scenarios. In this paper, we investigate the paradigm shift from deterministic regression toward generative regression. We propose the Multimodal Conditional Score-based Diffusion model for Regression (MCSDR), a probabilistic framework designed to model the continuous posterior distribution of LVEF conditioned on echocardiogram videos and patient demographic attribute priors. Extensive experiments conducted on the EchoNet-Dynamic, EchoNet-Pediatric, and CAMUS datasets demonstrate that MCSDR achieves state-of-the-art performance. Notably, qualitative analysis reveals that the generation trajectories of our model exhibit distinct behaviors in cases characterized by high noise or significant physiological variability, thereby offering a novel layer of interpretability for AI-aided diagnosis. Code will be available at <https://github.com/lvmarc/MCSDR.git>.

Index Terms—Left Ventricular Ejection Fraction, Generative Regression, Diffusion Models, Multimodal Fusion.

I. INTRODUCTION

Left Ventricular Ejection Fraction (LVEF) is a standard metric in cardiology for diagnosing heart failure and guiding therapeutic decisions [1–4]. The automation of LVEF assessment using deep learning has seen steady progress, with recent models achieving performance comparable to human experts on large-scale datasets [5–9]. However, the majority of existing approaches frame LVEF estimation as a standard deterministic regression problem, mapping an input video directly to a scalar value.

We posit that this deterministic formulation is mathematically suboptimal for echocardiography analysis due to the

This work is partially supported by National Natural Science Foundation of China (62376231), Fundamental Research Funds for the Central Universities (2682025ZTPY052, 2682023ZDPY001). (Corresponding authors: Xun Gong)

Jinrong Lv, Xun Gong, Weili Jiang are with the School of Computing and Artificial Intelligence, Southwest Jiaotong University, and the Manufacturing Industry Chain Collaboration Industrial Software Key Laboratory of Sichuan Province, Chengdu, Sichuan 610031, China (e-mail: lvjinrong@my.swjtu.edu.cn, lvjinrong.23@gmail.com; xgong@swjtu.edu.cn; jiangweili@swjtu.edu.cn, weili.jiang11@gmail.com, machong@swjtu.edu.cn).

ZhaoHuan Li are with the School of Medicine, University of Electronic Science and Technology, Chengdu, Sichuan 610031, China (e-mail: lzhjx2007@uestc.edu.cn).

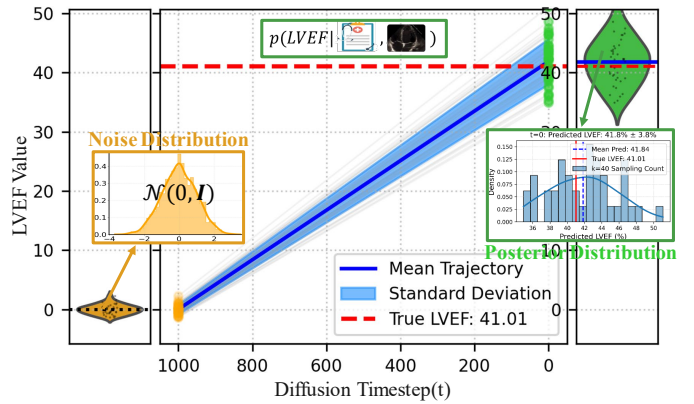


Fig. 1. Illustration of the proposed LVEF probabilistic inference process. The model reverses the diffusion process (blue), transforming random noise (orange) into plausible LVEF samples. Crucially, this trajectory is guided by the fusion of echocardiogram videos and patient demographic attributes (e.g., age, sex). By sampling multiple trajectories, we approximate the full posterior distribution (green). A narrow distribution indicates high confidence supported by unambiguous evidence, and vice versa.

ill-posed nature of the inverse problem. Ultrasound imaging is inherently plagued by speckle noise, acoustic artifacts, and variability in operator-dependent views. Consequently, a single observed video sequence x may not map to a unique ground truth y , but rather to a distribution of plausible physiological values. Standard regression models trained with Mean Squared Error (MSE) or Mean Absolute Error (MAE) loss theoretically converge to the conditional expectation $\mathbb{E}[y|x]$ [10]. While the mean is a statistically safe estimator, it can be misleading in medical contexts where the posterior distribution is multimodal or asymmetric. For instance, in cases of ambiguous wall motion, the conditional mean might yield an intermediate value that does not correspond to any valid pathological state, effectively blurring the diagnosis.

To address these challenges, we propose reframing LVEF estimation as a **Generative Regression** task. Instead of learning a direct mapping $f : \mathcal{X} \rightarrow \mathcal{Y}$, we aim to model the conditional posterior distribution $p(y|\mathcal{X}, \mathcal{A})$, where \mathcal{X} represents the visual data and \mathcal{A} denotes clinical priors. This probabilistic perspective allows for capturing the range of plausible outcomes given the evidence.

A second consideration regarding current *Feature Extractor + Regression Head* architectures is the integration of non-visual priors. In clinical practice, a diagnosis is often informed by more than images alone; patient attributes such as age, sex, and weight provide Bayesian priors that can help constrain the scope of diagnostic inference [11]. However, existing methodologies often overlook these readily available clinical

contextual data.

In this paper, we introduce the **Multimodal Conditional Score-based Diffusion model for Regression (MCSDR)**. Leveraging the theoretical framework of Stochastic Differential Equations (SDEs) [12–15], MCSDR learns to generate LVEF predictions by reversing a diffusion process. Starting from Gaussian noise, the model iteratively denoises the target variable, guided by a learned score function (gradient of the log-density). To effectively parameterize this score function, we specifically architect the **Multimodal Conditional Score Network (MCSN)**. By integrating high-dimensional spatiotemporal visual representations with low-dimensional patient demographic attributes, the MCSN enables clinical priors to modulate the underlying gradient field, thereby implicitly steering the stochastic trajectory toward the ground-truth manifold.

This generative formulation offers two potential advantages. First, we aim to enhance prediction accuracy. By approximating the full distribution rather than a single mean, the diffusion process effectively accommodates the non-Gaussian distributions prevalent in medical data. Second, this framework provides an intrinsic mechanism for reliability assessment. By sampling multiple trajectories from the learned posterior distribution, we can visualize the dispersion of the solution space. A narrow distribution indicates a well-posed solution supported by unambiguous evidence, whereas a dispersed distribution reflects high aleatoric uncertainty, suggesting that the prediction warrants expert review.

Our main contributions are summarized as follows:

- We introduce a diffusion-based framework for LVEF estimation, treating the task as a probabilistic inverse problem. This approach addresses the mean-regression tendency of deterministic models, allowing for the capture of complex posterior distributions.
- We design a conditioning mechanism that fuses high-dimensional echocardiogram features with tabular patient demographic attributes. This allows patient-specific priors to guide the solution of the inverse problem.
- We conduct comprehensive experiments on three public datasets: EchoNet-Dynamic, EchoNet-Pediatric, and CARMUS. MCSDR achieves state-of-the-art accuracy, particularly in challenging scenarios, and provides an interpretable analysis of prediction reliability.

II. RELATED WORK

A. Echocardiography Video Analysis and LVEF Estimation

Automated echocardiography video analysis has evolved from low-level signal processing to high-level semantic interpretation. Early methodologies focused on myocardial motion tracking using monogenic signals [16], optical flow [17], or sparse dictionary learning [18], alongside segmentation-based pipelines [19–21] for volumetric assessment. With the advent of deep learning, direct video regression became the mainstream paradigm. The seminal EchoNet-Dynamic [22] established the efficacy of 3D CNNs, an approach subsequently extended to diverse clinical scenarios [7, 23]. To better capture spatiotemporal dependencies, advanced architectures

like Transformers [5, 8] and Graph Neural Networks [6, 9] were introduced. Most recently, large-scale foundation models [11, 24] have emerged, offering generalized representations for cardiac analysis.

However, despite these advancements, the underlying paradigm remains predominantly deterministic. Existing methods typically model the conditional expectation $\mathbb{E}[y|x]$, treating physiological estimation as a fixed point-mapping task. This formulation overlooks the aleatoric uncertainty inherent in noisy ultrasound imagery. Our work departs from this convention by reframing the task as a probabilistic inverse problem, utilizing a generative approach to recover the full posterior distribution.

B. Score-Based Generative Model for Prediction

Score-based generative models learn the data distribution's score function—the gradient of its log-probability density—to guide generation [25–27]. This score is effectively learned via score matching [28] and its more robust variant, denoising score matching [29]. Early models improved sample quality using multi-scale noise [30], which, along with Denoising Diffusion Probabilistic Models (DDPMs) [12, 31], was unified under a stochastic differential equation (SDE) framework [14]. This framework revealed a deterministic generation process via an ordinary differential equation (ODE), enabling faster sampling with numerical solvers [13, 32, 33] and maximum likelihood training [34].

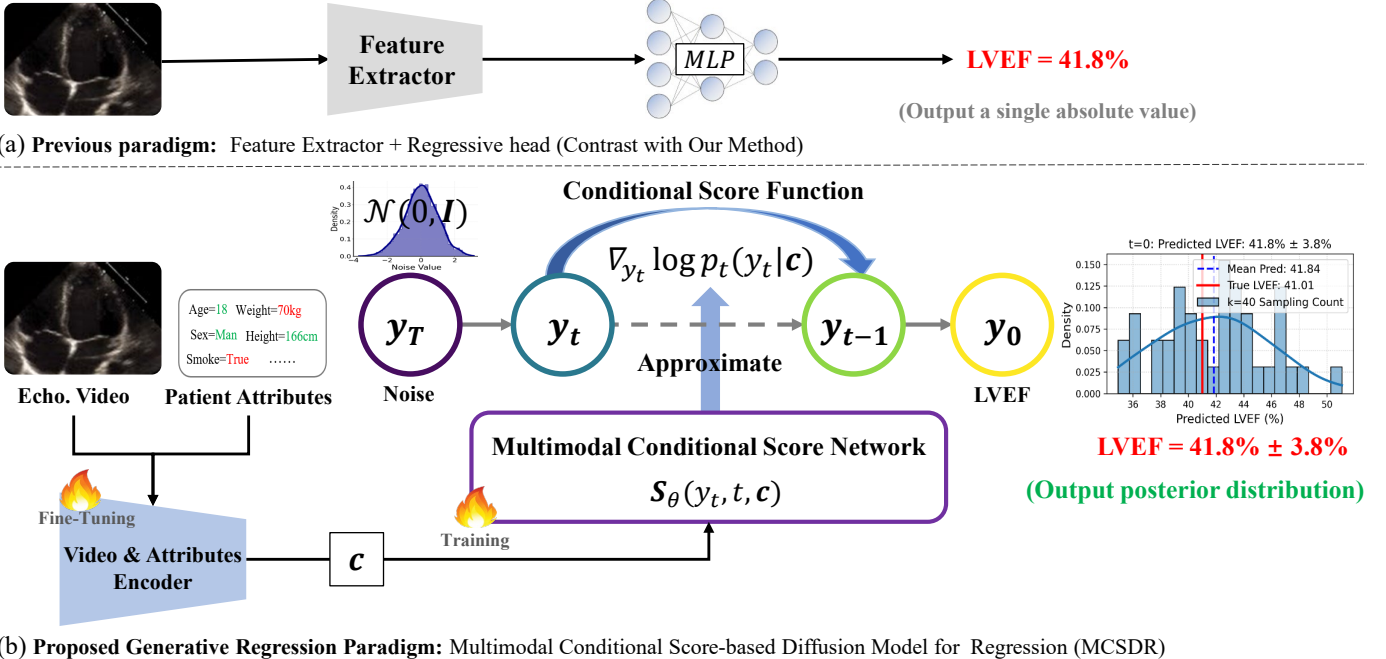
While originally designed for generation, the potential of diffusion models for discriminative tasks and regression is gaining attention. Unlike implicit models (e.g., GANs) or explicit density models (e.g., VAEs), diffusion models offer stable training and high-quality mode coverage. Recent studies have successfully adapted diffusion priors for time series imputation [35], trajectory forecasting [36]. Specifically, conditional diffusion models allow for the controlled generation of a target variable y given input covariates x . By learning the conditional score function $\nabla_y \log p(y|x)$, these models effectively convert regression into a conditional generation task. Inspired by these advances, we propose MCSDR, specifically tailoring the conditional score-based framework to handle the multimodal heterogeneity of clinical data for robust estimation.

III. METHOD

In this section, we articulate the proposed framework for solving the LVEF estimation inverse problem. We first rigorously define the probabilistic objective (Sec. III-A). We then detail the score-based generative dynamics used to traverse the solution manifold (Sec. III-B) and the Multimodal Conditional Score Network (MCSN) designed for heterogeneous prior fusion (Sec. III-C). Finally, we describe the inference procedure for posterior recovery (Sec. III-E).

A. Problem Formulation

Let $y \in \mathcal{Y} \subset \mathbb{R}$ denote the scalar physiological metric (LVEF), and $x \in \mathcal{X}$ denote the observed echocardiogram



(b) **Proposed Generative Regression Paradigm:** Multimodal Conditional Score-based Diffusion Model for Regression (MCSDR)

Fig. 2. **Paradigm shift from deterministic to generative regression.** (a) Conventional methods minimize MSE loss to predict a single point estimate (conditional mean), often failing to capture ambiguity. (b) Our proposed MCSDR framework treats LVEF estimation as a probabilistic inverse problem. It fuses the echocardiogram video with patient attributes to learn a conditional score function. This function guides a reverse diffusion process to generate the full posterior distribution $p(y|\mathbf{x}, \mathbf{c})$.

video. The imaging process can be conceptually modeled as a forward operator \mathcal{F} :

$$\mathbf{x} = \mathcal{F}(\mathbf{y}; \mathbf{z}) + \eta, \quad (1)$$

where \mathbf{z} represents unobserved latent factors (e.g., view angle, heart geometry) and η denotes measurement noise (e.g., speckle). The goal of LVEF estimation is to invert this process to recover \mathbf{y} .

However, this inverse problem is fundamentally *ill-posed*. Due to information loss in \mathcal{F} (projection from 3D motion to 2D planes) and the stochastic nature of η , the mapping $\mathbf{x} \mapsto \mathbf{y}$ is one-to-many. Deterministic regression, which minimizes $\|\hat{\mathbf{y}} - \mathbf{y}\|^2$, inherently targets the conditional expectation $\mathbb{E}[\mathbf{y}|\mathbf{x}]$. In multimodal distributions—common in pathological cases—the mean may fall in a low-density region of the true posterior, yielding an implausible estimate.

To address this, we formulate the task as estimating the full conditional posterior distribution $p(\mathbf{y}|\mathbf{x}, \mathbf{a})$. Here, $\mathbf{a} \in \mathcal{A}$ denotes patient demographic attributes (e.g., age, sex). From a Bayesian perspective, these attributes serve as **informative priors**. While the visual likelihood $p(\mathbf{x}|\mathbf{y})$ constrains the estimate based on motion, the demographic prior $p(\mathbf{y}|\mathbf{a})$ constrains the solution space to a physiologically probable range, effectively regularizing the ill-posed inversion:

$$p(\mathbf{y}|\mathbf{x}, \mathbf{a}) \propto p(\mathbf{x}|\mathbf{y}, \mathbf{a})p(\mathbf{y}|\mathbf{a}). \quad (2)$$

Our framework, MCSDR, implicitly learns this posterior using a score-based generative approach.

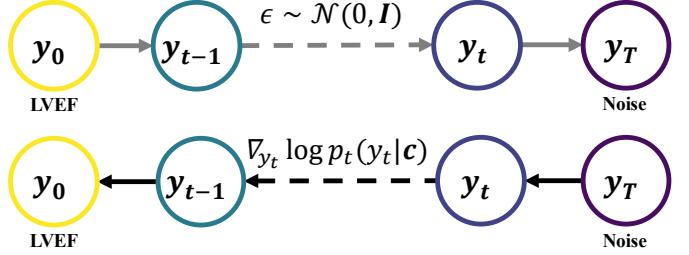


Fig. 3. **The stochastic generative trajectory.** Top: The forward diffusion process gradually perturbs the scalar LVEF label y_0 into Gaussian noise y_T . Bottom: The reverse generative process, governed by the learned conditional score function, iteratively solves the inverse problem to reconstruct y_0 from noise, conditioned on clinical evidence.

B. Score-Based Generative Dynamics

We leverage the continuous-time diffusion framework [14] to transform the regression task into a generative process. This involves two coupled stochastic differential equations (SDEs).

a) Forward Perturbation (Prior Construction): The forward process progressively diffuses the ground-truth physiological signal y_0 into noise, independent of conditioning variables. It is governed by the Variance Preserving (VP) SDE:

$$dy_t = -\frac{1}{2}\beta(t)y_t dt + \sqrt{\beta(t)}dw, \quad t \in [0, T], \quad (3)$$

where w is a standard Wiener process and $\beta(t)$ is a noise schedule. As $t \rightarrow T$, the distribution of y_t converges to a standard Gaussian prior $p_T(y) \approx \mathcal{N}(0, 1)$, effectively wiping out the original signal information.

b) Reverse Restoration (Manifold Recovery): The generative process corresponds to reversing the diffusion time from

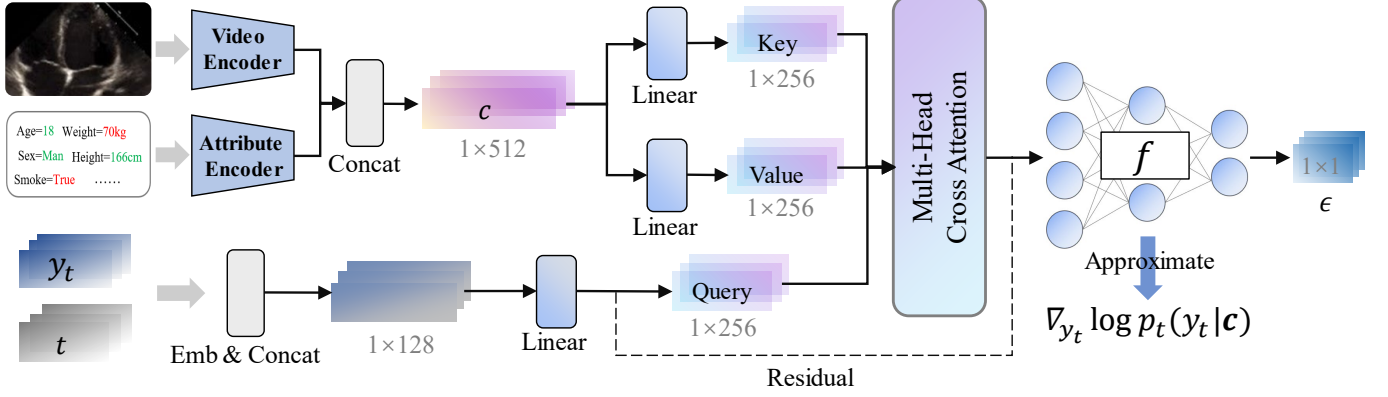


Fig. 4. **Architecture of the Multimodal Conditional Score Network (MCSN).** The network estimates the gradient field necessary for the generative process. To effectively fuse heterogeneous data, we employ dual encoders: a **Video Encoder** for spatiotemporal echocardiogram features and an **Attribute Encoder** for tabular clinical priors (e.g., age, weight). These features are concatenated and projected to form the Keys (**K**) and Values (**V**) in the cross-attention mechanism. This design allows the model to dynamically condition the denoising of the LVEF state (Query **Q**) on specific patient contexts.

T to 0. It is governed by the reverse-time SDE, or equivalently for deterministic sampling, the Probability Flow ODE [14]:

$$dy_t = \left[-\frac{1}{2}\beta(t)y_t - \frac{1}{2}\beta(t)\nabla_{y_t} \log p_t(y_t|\mathbf{c}) \right] dt. \quad (4)$$

where \mathbf{c} denotes the **unified multimodal embedding** derived from the raw inputs \mathbf{x} and \mathbf{a} (i.e., $\mathbf{c} = \text{Encoder}(\mathbf{x}, \mathbf{a})$). It is worth noting that unlike the reverse-time SDE which utilizes a score coefficient of $-\beta(t)$, the deterministic ODE formulation scales the score term by $-\frac{1}{2}\beta(t)$ to match the marginal densities without stochastic injection. The core term here is the **conditional score function** $\nabla_{y_t} \log p_t(y_t|\mathbf{c})$. Geometrically, this score represents a vector field (in 1D, a gradient) that points towards high-density regions of the conditional data distribution. By following this gradient field, we can traverse from the noise domain back to the physiological manifold. Since the true score is unknown, we approximate it using a time-dependent neural network $S_\theta(y_t, t, \mathbf{c})$, described below.

C. Multimodal Conditional Score Network (MCSN)

The accuracy of the inverse solution hinges on the quality of the estimated gradient field. We propose the MCSN architecture to effectively fuse the heterogeneous modalities—high-dimensional spatiotemporal video \mathbf{x} and low-dimensional tabular priors \mathbf{a} —to condition the score estimation.

a) *Heterogeneous Feature Encoding:* We employ a dual-branch encoder design to handle the distinct nature of the inputs:

- **Visual Encoder:** The echocardiogram video \mathbf{x} is processed by a pre-trained spatiotemporal backbone [8] to extract a dense visual embedding $\mathbf{h}_{vis} \in \mathbb{R}^{d_v}$. This vector encapsulates the motion patterns and structural deformations essential for the likelihood term $p(\mathbf{x}|y)$.
- **Attribute Encoder:** Tabular demographic attributes \mathbf{a} are processed via a Multi-Layer Perceptron (MLP) to project discrete and continuous variables into a latent semantic space $\mathbf{h}_{attr} \in \mathbb{R}^{d_a}$. This embedding encodes the Bayesian prior $p(y|\mathbf{a})$, providing demographic constraints.

b) *Dynamic Gradient Modulation via Attention:* To integrate these features, we treat the score estimation as a conditional modulation problem. The noisy state y_t is first embedded with sinusoidal time features to form the Query vector \mathbf{Q} . The visual and attribute embeddings are concatenated to form the context $\mathbf{c} = [\mathbf{h}_{vis}; \mathbf{h}_{attr}]$, which is projected into Keys \mathbf{K} and Values \mathbf{V} . We employ a Multi-Head Cross-Attention mechanism:

$$\text{Attention}(\mathbf{Q}, \mathbf{K}, \mathbf{V}) = \text{softmax} \left(\frac{\mathbf{Q}\mathbf{K}^T}{\sqrt{d_k}} \right) \mathbf{V}. \quad (5)$$

This mechanism allows the network to dynamically weigh the evidence. For instance, in frames where visual features are ambiguous (e.g., severe noise), the attention mechanism can attend more heavily to the demographic priors (\mathbf{h}_{attr}) to guide the gradient computation, thereby stabilizing the inverse solution.

D. Training Objective

Following the standard denoising score matching formulation [12], we train the network to predict the noise ϵ added to y_0 . The objective minimizes the MSE between the predicted noise and the actual noise:

$$\mathcal{L}(\theta) = \mathbb{E}_{t, y_0, \mathbf{c}, \epsilon} \left[\|\epsilon - \epsilon_\theta(y_t, t, \mathbf{c})\|^2 \right]. \quad (6)$$

Crucially, although we use an MSE loss on the *noise*, this is mathematically equivalent to minimizing the Fisher Divergence between the data distribution and the model distribution. This differs fundamentally from direct MSE regression on y , as it learns the structure of the distribution (the score) rather than just its mean.

E. Inference and Solution Analysis

During inference, our goal is to approximate the posterior $p_\theta(y|\mathbf{c})$. Since the exact analytical form is intractable, we employ a Monte Carlo sampling strategy.

a) *Deterministic Sampling via DDIM*: To ensure computational efficiency, we utilize the Denoising Diffusion Implicit Model (DDIM) solver [13]. By setting the variance parameter $\eta = 0$, the reverse process becomes deterministic. This allows us to solve the Probability Flow ODE (Eq. 4) with a reduced number of steps (e.g., $\tau = 10$), mapping a specific noise sample y_T uniquely to a predicted y_0 .

b) *Monte Carlo Posterior Approximation*: To capture the full solution space of the ill-posed inverse problem, we sample K independent trajectories starting from standard Gaussian noise $y_T^{(k)} \sim \mathcal{N}(0, 1)$ for $k = 1, \dots, K$. Each trajectory represents a plausible hypothesis consistent with the conditional evidence. The final estimate is derived from the empirical statistics of these hypotheses:

$$\hat{y} = \frac{1}{K} \sum_{k=1}^K \hat{y}_0^{(k)}, \quad \sigma = \sqrt{\frac{1}{K-1} \sum_{k=1}^K (\hat{y}_0^{(k)} - \hat{y})^2}. \quad (7)$$

Here, \hat{y} represents the ensemble prediction (approximating the posterior mean), while σ characterizes the dispersion of the solution space. A large σ indicates a flat or multimodal posterior landscape, signaling high ambiguity in the inverse problem (e.g., conflicting visual evidence), whereas a small σ indicates a sharp, well-posed solution.

IV. EXPERIMENTS

A. Datasets and Experimental Setup

We evaluate our framework on three public echocardiography datasets, chosen to represent varying degrees of clinical complexity and data modality availability.

EchoNet-Dynamic [22]. A large-scale dataset comprising 10,030 apical-4-chamber (A4C) echocardiogram videos. While it includes textual reports, these contain direct measurements (e.g., EDV, ESV) that would cause label leakage if used as input. Therefore, we utilize this dataset exclusively for **vision-only** experiments to benchmark the visual encoding capability of our model.

EchoNet-Pediatric [23]. A pediatric dataset containing 3,682 A4C videos from patients aged 0–18 years. This dataset presents significant challenges due to the high physiological variability across developmental stages. It includes tabular demographic attribute details (e.g., age, sex, weight, height), which we utilize as patient demographics for multimodal conditioning.

CAMUS [37]. A dataset containing 500 patients with both A2C and A4C views. It is characterized by variable image quality and potential artifacts, representing a challenging inverse problem scenario. Similar to EchoNet-Pediatric, we use the provided patient demographics as tabular priors.

Evaluation Metrics.

We employ standard deterministic metrics: Mean Absolute Error (MAE), Root Mean Squared Error (RMSE), and the Coefficient of Determination (R^2). Crucially, to evaluate the model’s ability to recover the true data distribution rather than just the conditional mean, we report the Continuous Ranked Probability Score (CRPS). CRPS generalizes MAE to probabilistic forecasts, measuring the distance between the

predicted posterior cumulative distribution function (CDF) and the empirical step function of the ground truth. Lower CRPS indicates better distributional fidelity.

B. Implementation Details

MCSDR is implemented in PyTorch. The video encoder utilizes a pre-trained Uniformer-Small [8] backbone, which is fine-tuned using a differential learning rate strategy (10% of the base LR). The diffusion process is governed by a Variance Preserving (VP) SDE with a linear $\beta(t)$ schedule ranging from 10^{-4} to 0.02 over $T = 1000$ discrete training steps. During training, we optimize the denoising objective (Eq. 6) using AdamW (LR 3×10^{-4} , weight decay 1×10^{-5}) on NVIDIA RTX 4090 GPUs. During inference, we approximate the posterior using the deterministic DDIM solver ($\eta = 0$) with $\tau = 10$ steps to balance precision and latency. The final prediction is the ensemble mean of $K = 40$ stochastic trajectories sampled from the standard Gaussian prior. For remaining technical specifics, please refer to our publicly released code (<https://github.com/lvmarch/MCSDR.git>).

C. Comparison with State-of-the-Art Methods

To rigorously evaluate the proposed generative paradigm, we compare MCSDR against a comprehensive set of baselines. These include traditional deterministic regression models employing diverse backbones—CNNs (EchoNet [22], FHFA-MTL [9]), Transformers (UVT [5], EchoCoTr [38], CoReEcho [8]), and Graph Neural Networks (EchoGNN [6], EchoGraphs [39])—as well as recent large-scale medical foundation models (EchoClip [11], PanEcho [24]).

Benchmark on Large-Scale Adult Echocardiography. Table I presents the results on the EchoNet-Dynamic test set. To ensure a strictly fair comparison and prevent potential label leakage from the dataset’s derived text attributes, our MCSDR model is evaluated in a vision-only mode. Despite utilizing only visual inputs, MCSDR establishes a new state-of-the-art, achieving an MAE of 3.76. Notably, it outperforms the recent foundation model PanEcho (MAE 5.35) and the latest multitask regression framework FHFA-MTL (MAE 3.89). This result suggests that the performance bottleneck in current LVEF estimation may not lie in the feature extractor’s capacity, but rather in the regression paradigm itself. By modeling the target as a distribution rather than a point estimate.

Benchmark on High-Variability Pediatric Data. The EchoNet-Pediatric dataset presents challenges stemming from high physiological variability across developmental stages (ages 0–18). As shown in Table 2, our approach outperforms all baselines, including data-release methods that benefit from extensive pre-training. Notably, incorporating patient demographics as conditional priors further improves R^2 from 0.74 to 0.77. This demonstrates that patient-specific demographics are highly beneficial for physiological metric prediction.

Benchmark on Small-Scale, Noisy Data. The CAMUS dataset represents a classic ill-posed inverse problem scenario, characterized by a small sample size ($N = 500$) and variable, often suboptimal, image quality. The results in Table III provide the most compelling evidence for our multimodal

TABLE I

COMPARISON WITH SOTA METHODS ON THE ECHONET-DYNAMIC. “-” INDICATES UNAVAILABLE RESULTS. “*” INDICATES REPRODUCIBLE SOURCE CODE.

Type	Method	MAE ↓	RMSE ↓	$R^2 \uparrow$
Foundation Model	EchoClip[11]	7.14	-	-
	PanEcho[24]	5.35	-	-
Deterministic Regression	*EchoNet(32F)[6]	4.22	5.56	0.79
	*UVT[5]	5.95	8.38	0.52
	*EchoGNN[6]	4.45	5.97	0.76
	*EchoGraphs[39]	4.01	5.36	0.81
	*EchoCoTr[38]	3.95	5.17	0.82
	Batool et al.[21]	5.74	7.73	0.60
	*CoReEcho[8]	3.90	5.13	0.82
	FHFA-MTL[9]	3.89	5.13	0.82
Generative Regression	MCSDR (Vision only)	3.76	4.81	0.84

TABLE II

COMPARISON WITH SOTA METHODS ON THE ECHONET-PEDIATRIC.

Method	MAE ↓	RMSE ↓	$R^2 \uparrow$
*UVT[5]	7.91	9.47	0.33
*EchoGNN[6]	5.69	7.28	0.60
*EchoGraphs[39]	5.29	6.87	0.65
*EchoCoTr[38]	4.82	6.26	0.71
*CoReEcho[8]	4.70	6.40	0.69
MCSDR (Vision only)	4.26	5.88	0.74
MCSDR (Vision + Demographic)	4.22	5.59	0.77

TABLE III

COMPARISON WITH SOTA METHODS ON THE CAMUS.

Method	MAE ↓	RMSE ↓	$R^2 \uparrow$
UVT[5]	9.42	11.02	0.27
EchoGNN[6]	8.58	9.73	0.43
EchoGraphs[39]	8.70	9.66	0.44
EchoCoTr[38]	7.38	8.99	0.51
CoReEcho[8]	7.35	8.76	0.54
MCSDR (Vision only)	6.22	8.31	0.58
MCSDR (Vision + Demographic)	5.73	7.50	0.66

generative formulation. Deterministic baselines degrade significantly in this setting, with CoReEcho yielding an MAE of 7.35. Our vision-only MCSDR significantly reduces this error to 6.22, demonstrating the data efficiency of the diffusion training objective. Most importantly, the fusion of patient demographics brings a substantial performance leap, further reducing the MAE to 5.73. This empirical evidence validates our core hypothesis: when visual evidence is ambiguous due to noise or artifacts, the generative process effectively leverages clinical priors to constrain the solution space, guiding the trajectory toward the ground truth.

D. Visual and Distribution Analysis

To substantiate the quantitative metrics, we provide a qualitative assessment of the model’s predictive behavior in Figure 5. The visualization consists of scatter plots (Left)

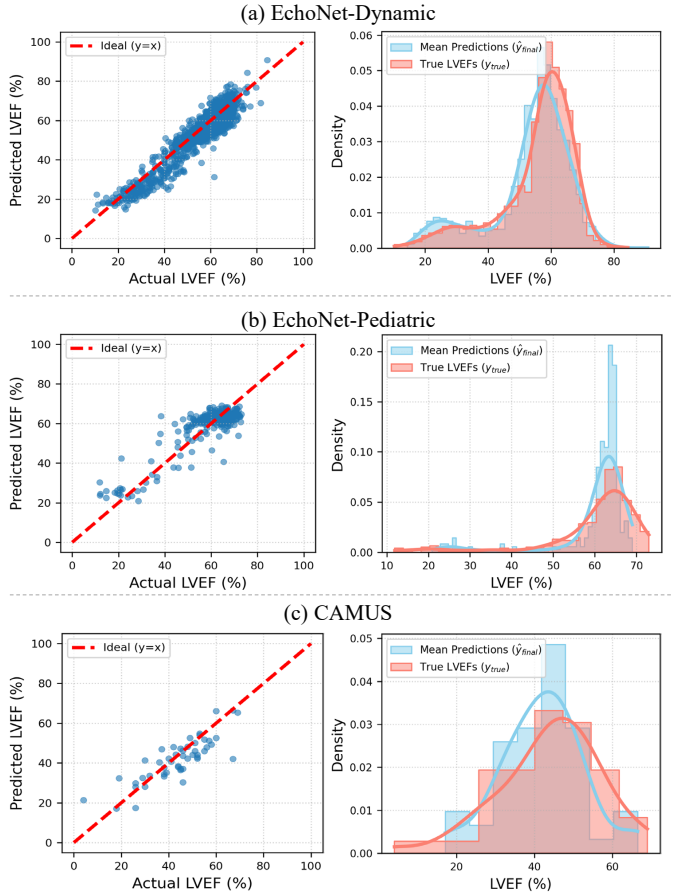


Fig. 5. Visual analysis of model predictions on (a) CAMUS, (b) EchoNet-Pediatric, and (c) EchoNet-Dynamic test sets. Left: Scatter plots of Predicted vs. True LVEF. Right: Density plots comparing the distribution of predictions (Blue) against the ground truth (Red).

illustrating instance-level accuracy and density plots (Right) evaluating population-level distributional fidelity.

Instance-Level Alignment. On the large-scale EchoNet-Dynamic dataset (Fig. 5a), the predictions exhibit remarkable tightness around the ideal identity line ($y = x$), correlating with the high R^2 of 0.84. For the EchoNet-Pediatric dataset (Fig. 5b), despite the high physiological variability inherent in the 0–18 age range, the scatter plot maintains a linear trajectory with minimal outliers. Even on the challenging CAMUS dataset (Fig. 5c), where image quality is suboptimal, the predictions remain unbiased. The increased dispersion observed in the CAMUS scatter plot correctly reflects the higher aleatoric uncertainty associated with noisy inputs, rather than systematic model failure.

Distributional Fidelity. A common pitfall in deterministic regression is the tendency to collapse towards the conditional mean, often resulting in a predicted distribution that is narrower than the ground truth (i.e., underestimating the variance of the population). In contrast, the density plots in the right column demonstrate that MCSDR preserves the true statistical properties of the target variable. As shown in Fig. 5a and b, the probability density functions of our mean predictions (Blue) align almost perfectly with the ground truth densities (Red). Notably, on EchoNet-Pediatric, the model accurately

TABLE IV
ABLATION ON PARADIGM EFFECTIVENESS AND COMPUTATIONAL COST.

Method	MAE	RMSE	R ²	FLOPs	Time
Deterministic Reg.	5.26	6.85	0.65	~13.8G	0.01s
MCSDR (DDPM)	4.20	5.69	0.75	~69.1G	1.17s
MCSDR (DDIM)	4.13	5.55	0.77	~14.4G	0.02s

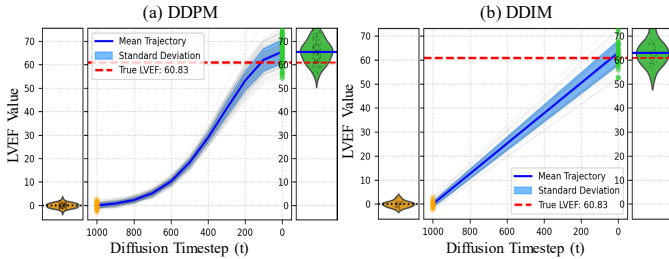


Fig. 6. Visual comparison of sampling trajectories. Top: Stochastic DDPM path ($T = 1000$). Bottom: Deterministic DDIM path ($\tau = 10$). The nearly linear trajectory of the ODE-based DDIM allows for efficient sampling with fewer steps.

reproduces the high kurtosis (sharp peak) centered around 65% LVEF. On CAMUS, it successfully captures the broader, more platykurtic distribution. This generative consistency confirms that our probabilistic formulation effectively learns the underlying data manifold, ensuring that the generated LVEF values are not only accurate for individual patients but also statistically valid across the cohort.

E. Ablation Studies

1) *Generative vs. Deterministic Regression*: We first validate the core hypothesis that formulating regression as a generative task is beneficial. We compare MCSDR against a baseline that uses the exact same encoder backbone (Uniformer + Attribute MLP) but is trained with a standard regression head and MSE loss. As shown in Table IV, the generative formulation (using DDIM) improves MAE from 5.26 to 4.13 on EchoNet-Pediatric. This supports our premise that learning the gradient field of the data distribution allows for more robust inference than directly regressing the conditional mean, particularly for complex inverse problems.

2) *Sampler Selection: DDPM vs. DDIM*: We compare two sampling strategies for solving the reverse SDE/ODE. Table IV highlights the trade-off. While the stochastic DDPM sampler ($T = 1000$) achieves competitive accuracy, it incurs high latency (1.17s per sample). The deterministic DDIM sampler ($\eta = 0, \tau = 10$) achieves comparable or slightly better accuracy (MAE 4.13) but with drastically reduced inference time (0.02s). This efficiency is attributed to the semi-linear nature of the Probability Flow ODE trajectory (visualized in Figure 6), which allows for larger integration steps without significant discretization error.

3) *Architecture Effectiveness*: We further validate the design of the MCSN by comparing it with a simple MLP predictor and a Transformer Decoder. Table V shows that our dual-encoder MCSN architecture achieves the lowest CRPS (3.01) and MAE with significantly fewer parameters (0.69M)

TABLE V
ABLATION STUDY ON THE NOISE PREDICTOR ARCHITECTURE.

Architecture	MAE ↓	RMSE ↓	R ² ↑	CRPS ↓	Params.
<i>Results using DDPM Sampler ($T=1000$ steps)</i>					
MLP	4.73	6.48	0.68	3.71	0.23M
T-Decoder	4.43	5.55	0.77	3.28	2.27M
MCSN	4.20	5.69	0.75	3.04	0.69M
<i>Results using DDIM Sampler ($S=10$ steps)</i>					
MLP	4.27	5.79	0.74	3.10	0.23M
T-Decoder	4.30	5.87	0.74	3.04	2.27M
MCSN	4.13	5.55	0.77	3.01	0.69M

Figure 7 consists of two line plots. The left plot shows Metric Value (y-axis, 2 to 6) versus Diffusion Timestep (t) (x-axis, 5 to 500). It includes three data series: MAE (blue circles), CRPS (green triangles), and RMSE (orange squares). A red dashed vertical line marks t=10. The right plot shows Metric Value (y-axis, 2 to 6) versus Sampling Count (k) (x-axis, 5 to 500). It also includes MAE, CRPS, and RMSE. A red dashed vertical line marks k=40. Both plots show that performance is stable and improves as the number of steps or samples increases.

Fig. 7. The impact of key MCSDR hyperparameters.

compared to the Transformer Decoder (2.27M). This indicates that the specific design for fusing spatiotemporal features with tabular attributes is parameter-efficient.

4) *Impact of Key Hyperparameters*: We analyze the impact of the DDIM sampling steps (t) and the posterior sampling count (K) on the EchoNet-Pediatric dataset. Figure 7 (left) shows that model performance (MAE, RMSE, CRPS) is optimal at only 10 sampling steps. Using more steps provides no benefit and increases computational cost. Figure 7 (right) shows that performance rapidly improves as the sampling count K increases. The metrics stabilize around $K = 40$, indicating that a stable posterior approximation has been achieved. Based on this, we select $t = 10$ and $K = 40$ as our optimal configuration, achieving the best balance of accuracy and efficiency.

F. Qualitative Analysis of Generative Dynamics

Beyond deterministic accuracy, a key property of our score-based framework is its transparency. By visualizing the generative trajectories solving the probability flow ODE, we can interpret how the model navigates the inverse solution space given different levels of clinical ambiguity.

Posterior Adaptability to Input Ambiguity. Figure 8 demonstrates the model's ability to adapt the shape of its predicted posterior distribution $p_\theta(y|c)$ according to the quality of the visual evidence. For standard, high-quality echocardiograms (Fig. 8a), the model generates a sharp, unimodal distribution (std dev $\approx 4\%$), indicating a high-confidence consensus among the sampled hypotheses. In contrast, when the input is degraded by noise (Fig. 8b) or presents atypical cardiac anatomy (Fig. 8c), the posterior naturally dilates (std dev $> 10\%$). This phenomenon confirms that the variance in our regression head is not random noise, but a calibrated response to the *ill-posedness* of the specific input sample.

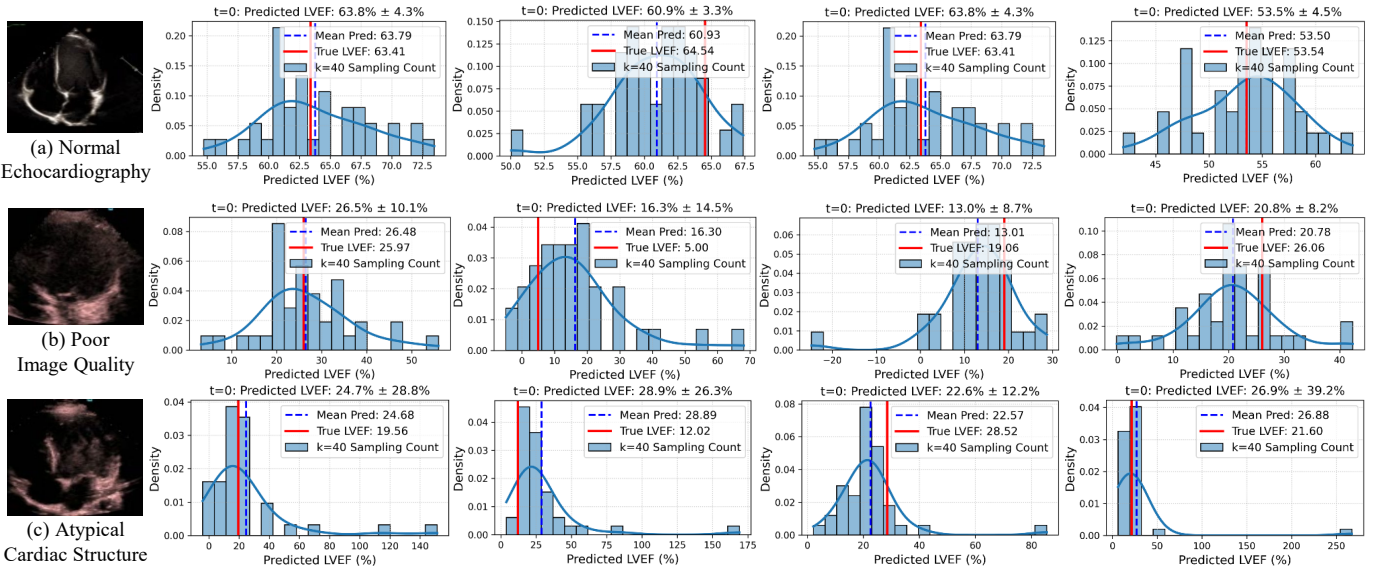


Fig. 8. **Posterior Adaptability.** The model’s output distribution adapts to clinical ambiguity. (a) High-quality inputs yield sharp posteriors. (b-c) Noisy or atypical inputs result in dispersed posteriors.

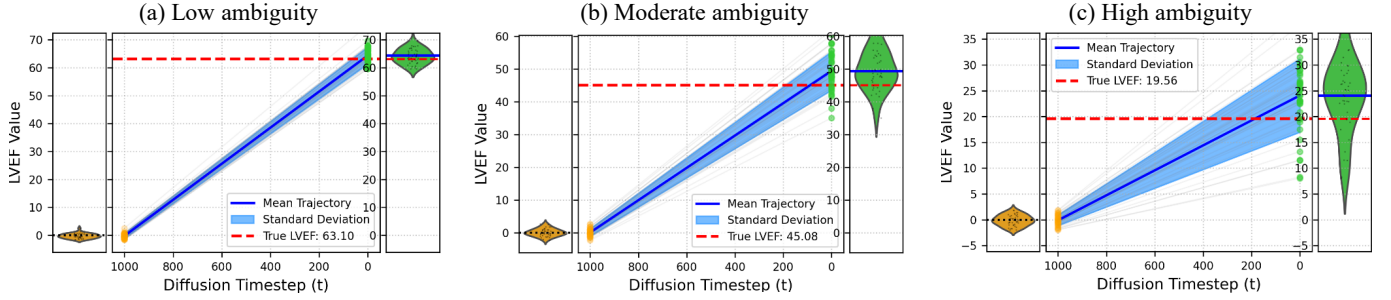


Fig. 9. **Trajectory Coherence Analysis.** The DDIM trajectories ($t = T \rightarrow 0$) reveal the geometry of the optimization landscape. (a) Coherent convergence implies a well-posed solution driven by strong visual evidence. (c) Trajectory dispersion faithfully reflects the ambiguity (ill-posedness) of the input, serving as an intrinsic reliability indicator.

Trajectory Coherence and Bifurcation. To further understand the origin of this variance, we visualize the DDIM sampling trajectories in Figure 9. In low-uncertainty cases (Fig. 9a), we observe strong **trajectory coherence**: despite starting from diverse random noise states y_T , the conditional score function acts as a powerful attractor, guiding all paths to converge rapidly into a tight bundle at $t = 0$. This indicates a steep, well-defined optimization landscape. Conversely, in high-uncertainty scenarios (Fig. 9c), the trajectories exhibit **bifurcation** or fanning. The score fields in these regions are flatter or multi-modal, allowing different noise initializations to drift towards disparate solutions.

Visualizing Failure Modes. The red arrows in Figure 10 highlight a phenomenon of conditional guidance failure. In these challenging cases, the learned gradient field is too weak to uniformly guide all initialization points towards the central mode. Consequently, a subset of trajectories—originating from specific regions of the Gaussian prior—diverges significantly from the main cluster. This divergence suggests that the conditional probability landscape is flat or multi-modal, meaning the evidence supports multiple potential interpretations.

V. DISCUSSION

In this work, we proposed a paradigm shift from deterministic to generative regression for LVEF estimation. While the experimental results demonstrate state-of-the-art performance, several aspects regarding clinical practicality, model behavior, and limitations warrant deeper discussion.

A. Computational Cost vs. Clinical Safety

A valid concern arises regarding the inference latency introduced by the generative process. As noted in Table 5 (in Experiments), while a single DDIM step is extremely fast (0.02s), estimating a reliable posterior distribution requires sampling K trajectories (e.g., $K = 40$). A sequential execution would indeed imply a total latency of roughly 0.8s per patient, which is higher than the 0.01s of a deterministic baseline.

We argue that this computational trade-off is both justifiable and negligible in clinical practice for two primary reasons. First, the K stochastic trajectories are strictly independent given the condition c , allowing them to be processed as a single batch operation on modern GPUs. Because our MCSN architecture is exceptionally lightweight, with only 0.69M

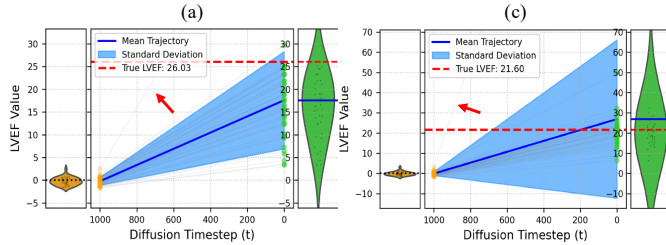


Fig. 10. **Failure Mode Visualization.** In high-error cases, the conditional guidance is often insufficient to unify the paths. Red arrows highlight divergent trajectories that break away from the main cluster, serving as a visual indicator of low reliability.

parameters, increasing the batch size from 1 to 40 incurs minimal overhead; thus, the total wall-clock time remains well within real-time requirements at less than 0.1s. Second, in high-stakes medical decision-making, the cost of a misdiagnosis far outweighs any marginal increase in computing time. While a deterministic model might execute in 0.01s, its inability to signal failure on noisy inputs poses a severe safety risk. Conversely, our framework operates in sub-second time while explicitly flagging unreliable predictions through high variance. We posit that this safety buffer is an essential requirement for trustworthy AI deployment, validating the modest increase in computational demand.

B. Physiological Boundaries in Gaussian Diffusion

Our current diffusion framework operates in an unbounded Gaussian space. Consequently, there is no inherent mathematical constraint preventing the generated scalar \hat{y} from falling outside the physiological range of LVEF (i.e., $[0, 100]$). In our experiments, we observed that for atypical hearts, the model occasionally predicts values slightly exceeding 100%.

This phenomenon stems from the tail behavior of the Gaussian prior. While one could impose bounded activations (e.g., Sigmoid) or truncated diffusion schemes, these often introduce gradient vanishing issues or complicate the score matching objective. In practice, we find that a simple post-hoc operation—clipping the final mean prediction to $[0, 100]$ —is sufficient and does not degrade performance. Importantly, the occurrence of out-of-bound samples is often informative in itself: it typically correlates with high aleatoric uncertainty, suggesting that the model is struggling to locate the exact manifold of the data due to extreme input features.

C. Limitations and Future Directions

Despite the promising results, our study has limitations that outline directions for future research.

Dependency on Complete Modalities. Our dual-encoder architecture currently assumes the availability of both visual data and tabular attributes. In clinical practice, demographic records may occasionally be incomplete (the missing modality problem). Currently, our model processes attributes as a holistic vector. Future work will explore modality-dropout training strategies to enhance robustness against missing clinical priors.

2D vs. 3D Assessment. Like most deep learning approaches in this domain, MCSDR estimates LVEF from 2D video slices

(A4C view). While this is the clinical standard for initial assessment, it relies on geometric assumptions about the left ventricle. Extending our conditional score-based framework to 3D echocardiography could theoretically provide a more direct volumetric assessment, provided that the scarcity of labeled 3D datasets can be addressed.

VI. CONCLUSION

This paper presents the Multimodal Conditional Score-based Diffusion model for Regression (MCSDR), a novel framework that reformulates LVEF estimation as a probabilistic generative task. Recognizing that extracting scalar metrics from noisy ultrasound images is inherently an ill-posed inverse problem, we move beyond the limitations of deterministic point estimation to model the full conditional posterior distribution of the target variable. Our methodology introduces the Multimodal Conditional Score Network (MCSN), which is specifically designed to integrate high-dimensional spatiotemporal visual representations with tabular clinical priors. This architecture allows the model to leverage demographic context to constrain the solution space, guiding the diffusion-based sampling process toward a robust recovery of ground-truth LVEF values. Extensive experiments conducted on three diverse datasets—EchoNet-Dynamic, EchoNet-Pediatric, and CAMUS—demonstrate that MCSDR achieves new state-of-the-art performance. Furthermore, by visualizing generative trajectories and posterior landscapes, our framework provides a novel interpretable perspective for reliable physiological signal assessment.

REFERENCES

- [1] J. F. POMBO, B. L. TROY, and R. O. RUSSELL, “Left ventricular volumes and ejection fraction by echocardiography,” *Circulation*, vol. 43, no. 4, pp. 480–490, 1971.
- [2] J. P. Curtis, S. I. Sokol, Y. Wang, S. S. Rathore, D. T. Ko, F. Jadbabaie, E. L. Portnay, S. J. Marshalko, M. J. Radford, and H. M. Krumholz, “The association of left ventricular ejection fraction, mortality, and cause of death in stable outpatients with heart failure,” *JACC*, vol. 42, no. 4, pp. 736–742, 2003.
- [3] M. T. Maeder and D. M. Kaye, “Heart failure with normal left ventricular ejection fraction,” *JACC*, vol. 53, no. 11, pp. 905–918, 2009.
- [4] S. Rosch, K.-P. Kresoja, C. Besler, K. Fengler, A. R. Schöber, M. von Roeder, C. Lücke, M. Gutberlet, K. Klingel, H. Thiele, K.-P. Rommel, and P. Lurz, “Characteristics of heart failure with preserved ejection fraction across the range of left ventricular ejection fraction,” *Circulation*, vol. 146, no. 7, pp. 506–518, 2022.
- [5] H. Reynaud, A. Vlontzos, B. Hou, A. Beqiri, P. Leeson, and B. Kainz, “Ultrasound video transformers for cardiac ejection fraction estimation,” in *Medical Image Computing and Computer Assisted Intervention – MICCAI 2021* (M. de Bruijne, P. C. Cattin, S. Cotin, N. Padoy, S. Speidel, Y. Zheng, and C. Essert, eds.), (Cham), pp. 495–505, Springer International Publishing, 2021.

[6] M. Mokhtari, T. Tsang, P. Abolmaesumi, and R. Liao, “Echognn: Explainable ejection fraction estimation with graph neural networks,” in *Medical Image Computing and Computer Assisted Intervention – MICCAI 2022* (L. Wang, Q. Dou, P. T. Fletcher, S. Speidel, and S. Li, eds.), (Cham), pp. 360–369, Springer Nature Switzerland, 2022.

[7] W. Dai, X. Li, X. Ding, and K.-T. Cheng, “Cyclical self-supervision for semi-supervised ejection fraction prediction from echocardiogram videos,” *IEEE Transactions on Medical Imaging*, vol. 42, no. 5, pp. 1446–1461, 2023.

[8] F. A. Maani, N. Saeed, A. Matsun, and M. Yaqub, “Coreecho: Continuous representation learning for 2d+time echocardiography analysis,” in *Medical Image Computing and Computer Assisted Intervention – MICCAI 2024* (M. G. Linguraru, Q. Dou, A. Feragen, S. Giannarou, B. Glocker, K. Lekadir, and J. A. Schnabel, eds.), (Cham), pp. 591–601, Springer Nature Switzerland, 2024.

[9] H. Mo, J. Liang, B. Li, Z. Hu, M. Yi, H. Wu, Q. Rong, and Z. Xu, “A noninvasive framework for heart function assessment by multitask learning,” *IEEE Transactions on Instrumentation and Measurement*, vol. 74, pp. 1–13, 2025.

[10] C. M. Bishop and N. M. Nasrabadi, *Pattern recognition and machine learning*, vol. 4. Springer, 2006.

[11] M. Christensen, M. Vukadinovic, N. Yuan, and D. Ouyang, “Vision–language foundation model for echocardiogram interpretation,” *Nature Medicine*, pp. 1–8, 2024.

[12] J. Ho, A. Jain, and P. Abbeel, “Denoising diffusion probabilistic models,” in *Advances in Neural Information Processing Systems*, vol. 33, pp. 6840–6851, 2020.

[13] C. M. iaming Song and S. Ermon, “Denoising diffusion implicit models,” in *International Conference on Learning Representations (ICLR)*, 2021.

[14] Y. Song, J. Sohl-Dickstein, D. P. Kingma, A. Kumar, S. Ermon, and B. Poole, “Score-based generative modeling through stochastic differential equations,” in *International Conference on Learning Representations (ICLR)*, 2021.

[15] Y. Chen, Q. Qu, and L. Shen, “Harnessing low dimensionality in diffusion models: From theory to practice,” 2025. International Conference on Learning Representations.

[16] M. Alessandrini, A. Basarab, H. Liebgott, and O. Bernard, “Myocardial motion estimation from medical images using the monogenic signal,” *IEEE Transactions on Image Processing*, vol. 22, no. 3, pp. 1084–1095, 2013.

[17] M. Suhling, M. Arigovindan, C. Jansen, P. Hunziker, and M. Unser, “Myocardial motion analysis from b-mode echocardiograms,” *IEEE Transactions on Image Processing*, vol. 14, no. 4, pp. 525–536, 2005.

[18] N. Ouzir, A. Basarab, H. Liebgott, B. Harbaoui, and J.-Y. Tourneret, “Motion estimation in echocardiography using sparse representation and dictionary learning,” *IEEE Transactions on Image Processing*, vol. 27, no. 1, pp. 64–77, 2018.

[19] S. Leclerc, E. Smistad, T. Grenier, C. Lartizien, A. Ostvik, F. Cervenansky, F. Espinosa, T. Espeland, E. A. Rye Berg, P.-M. Jodoin, L. Lovstakken, and O. Bernard, “Ru-net: A refining segmentation network for 2d echocardiography,” in *2019 IEEE International Ultrasonics Symposium (IUS)*, pp. 1160–1163, 2019.

[20] F. Maani, A. Ukaye, N. Saadi, N. Saeed, and M. Yaqub, “Simlvseg: Simplifying left ventricular segmentation in 2-d+time echocardiograms with self- and weakly supervised learning,” *Ultrasound in Medicine & Biology*, vol. 50, no. 12, pp. 1945–1954, 2024.

[21] S. Batool, I. A. Taj, and M. Ghafoor, “Ejection fraction estimation from echocardiograms using optimal left ventricle feature extraction based on clinical methods,” *Diagnostics*, vol. 13, no. 13, 2023.

[22] D. Ouyang, B. He, A. Ghorbani, N. Yuan, J. Ebinger, C. P. Langlotz, P. A. Heidenreich, R. A. Harrington, D. H. Liang, E. A. Ashley, *et al.*, “Video-based ai for beat-to-beat assessment of cardiac function,” *Nature*, vol. 580, no. 7802, pp. 252–256, 2020.

[23] C. D. Reddy, L. Lopez, D. Ouyang, J. Y. Zou, and B. He, “Video-based deep learning for automated assessment of left ventricular ejection fraction in pediatric patients,” *Journal of the American Society of Echocardiography*, vol. 36, no. 5, pp. 482–489, 2023.

[24] G. Holste, E. K. Oikonomou, M. Tokodi, A. Kovács, Z. Wang, and R. Khera, “Complete ai-enabled echocardiography interpretation with multitask deep learning,” *JAMA*, vol. 334, pp. 306–318, 07 2025.

[25] Y. Song and S. Ermon, “Generative modeling by estimating gradients of the data distribution,” *Advances in Neural Information Processing Systems*, vol. 32, 2019.

[26] B. Efron, “Tweedie’s formula and selection bias,” *Journal of the American Statistical Association*, vol. 106, no. 496, pp. 1602–1614, 2011.

[27] J. Sohl-Dickstein, E. Weiss, N. Maheswaranathan, and S. Ganguli, “Deep unsupervised learning using nonequilibrium thermodynamics,” in *International Conference on Machine Learning (ICML)*, pp. 2256–2265, PMLR, 2015.

[28] A. Hyvärinen and P. Dayan, “Estimation of non-normalized statistical models by score matching,” *Journal of Machine Learning Research*, vol. 6, no. 4, 2005.

[29] P. Vincent, “A connection between score matching and denoising autoencoders,” *Neural Computation*, vol. 23, no. 7, pp. 1661–1674, 2011.

[30] Y. Song, S. Garg, J. Shi, and S. Ermon, “Sliced score matching: A scalable approach to density and score estimation,” in *Proceedings of the 36th Conference on Uncertainty in Artificial Intelligence (UAI)*, pp. 574–584, PMLR, 2020.

[31] Y. Song and S. Ermon, “Improved techniques for training score-based generative models,” in *Advances in Neural Information Processing Systems*, vol. 33, pp. 12438–12448, 2020.

[32] C. Lu, Y. Zhou, F. Bao, J. Chen, C. Li, and J. Zhu, “Dpm-solver: A fast ode solver for diffusion probabilistic model

sampling in around 10 steps,” in *Advances in Neural Information Processing Systems*, vol. 35, pp. 5775–5787, 2022.

[33] C. Lu, Y. Zhou, F. Bao, J. Chen, C. Li, and J. Zhu, “Dpm-solver++: Fast solver for guided sampling of diffusion probabilistic models,” *Machine Intelligence Research*, pp. 1–22, 2025.

[34] Y. Song, C. Durkan, I. Murray, and S. Ermon, “Maximum likelihood training of score-based diffusion models,” in *Advances in Neural Information Processing Systems*, vol. 34, pp. 1415–1428, 2021.

[35] Y. Tashiro, J. Song, Y. Song, and S. Ermon, “CSDI: Conditional score-based diffusion models for probabilistic time series imputation,” in *Advances in Neural Information Processing Systems*, vol. 34, pp. 24804–24816, 2021.

[36] L. Zhang, A. Rao, and M. Agrawala, “Adding conditional control to text-to-image diffusion models,” in *Proceedings of the IEEE/CVF International Conference on Computer Vision (ICCV)*, pp. 3836–3847, 2023.

[37] S. Leclerc, E. Smistad, J. Pedrosa, A. Østvik, F. Cervenansky, F. Espinosa, T. Espeland, E. A. R. Berg, P.-M. Jodoin, T. Grenier, C. Lartizien, J. D’hooge, L. Lovstakken, and O. Bernard, “Deep learning for segmentation using an open large-scale dataset in 2d echocardiography,” *IEEE Transactions on Medical Imaging*, vol. 38, no. 9, pp. 2198–2210, 2019.

[38] R. Muhtaseb and M. Yaqub, “Echocotr: Estimation of the left ventricular ejection fraction from spatiotemporal echocardiography,” in *Medical Image Computing and Computer Assisted Intervention – MICCAI 2022* (L. Wang, Q. Dou, P. T. Fletcher, S. Speidel, and S. Li, eds.), (Cham), pp. 370–379, Springer Nature Switzerland, 2022.

[39] S. Thomas, A. Gilbert, and G. Ben-Yosef, “Light-weight spatio-temporal graphs for segmentation and ejection fraction prediction in cardiac ultrasound,” in *Medical Image Computing and Computer Assisted Intervention – MICCAI 2022* (L. Wang, Q. Dou, P. T. Fletcher, S. Speidel, and S. Li, eds.), (Cham), pp. 380–390, Springer Nature Switzerland, 2022.